Measuring kinetic inductance and superfluid stiffness of two-dimensional superconductors using high-quality transmission-line resonators

Mary Kreidel,[1] Xuanjing Chu,[2] Jesse Balgley,[3] Abhinandan Antony,[3] Nishchhal Verma,[4] Julian Ingham,[4] Leonardo Ranzani,[5] Raquel Queiroz,[4,6] Robert M. Westervelt,[1,7] James Hone,[3] and Kin Chung Fong[5,*]

[1]*School of Engineering and Applied Sciences, Harvard University, Cambridge, Massachusetts 02138, USA*
[2]*Department of Applied Physics and Applied Mathematics, Columbia University, New York, New York 10027, USA*
[3]*Department of Mechanical Engineering, Columbia University, New York, New York 10027, USA*
[4]*Department of Physics, Columbia University, New York, New York 10027, USA*
[5]*RTX BBN Technologies, Quantum Engineering and Computing Group, Cambridge, Massachusetts 02138, USA*
[6]*Center for Computational Quantum Physics, Flatiron Institute, New York, New York 10010, USA*
[7]*Department of Physics, Harvard University, Cambridge, Massachusetts 02138, USA*

(Received 12 July 2024; accepted 21 October 2024; published 6 December 2024)

The discovery of van der Waals superconductors in recent years has generated a lot of excitement for their potentially novel pairing mechanisms. However, their typical atomic-scale thickness and micrometer-scale lateral dimensions impose severe challenges to investigations of pairing symmetry by conventional methods. We demonstrate an improved technique that employs high-quality-factor superconducting resonators to measure the kinetic inductance—up to one part per million—and loss of a van der Waals superconductor. We analyze the equivalent circuit model to extract the kinetic inductance, superfluid stiffness, penetration depth, and ratio of imaginary and real parts of the complex conductivity. We validate the technique by measuring aluminum and finding excellent agreement in both the zero-temperature superconducting gap as well as the complex conductivity data when compared with BCS theory. We then demonstrate the utility of the technique by measuring the kinetic inductance of multilayered niobium diselenide and discuss the limits to the accuracy of our technique when the transition temperature of the sample, $NbSe_2$ at 7.06 K, approaches our Nb probe resonator at 8.59 K. Our method will be useful for practitioners in the growing fields of superconducting physics, materials science, and quantum sensing, as a means of characterizing superconducting circuit components and studying pairing mechanisms of the novel superconducting states which arise in layered two-dimensional materials and heterostructures.

DOI: 10.1103/PhysRevResearch.6.043245

I. INTRODUCTION

The confluence of flat bands, quantum geometry, and correlations gives rise to novel quantum phenomena in two-dimensional van der Waals (vdW) materials. For example, unconventional superconducting states have been observed in transition-metal dichalcogenides (TMDs), as well as twisted and untwisted multilayers of graphene and TMDs [1–15]. Accumulating evidence points to the unusual nature of both the superconducting pairing [16–18] and the normal parent state of these systems [19–21], demanding further experimental scrutiny. Superfluid stiffness is a fundamental quantity which gives insight into the nature of the pairing symmetry, and whose magnitude determines the relevance of phase fluctuations of the superconducting order parameter—of particular importance in strongly correlated superconductors characterized by low superfluid densities [22]. The superfluid stiffness is directly related to the London penetration depth λ_L, which characterizes the decay of an external magnetic field inside a superconductor due to the Meissner effect, and is traditionally a well-established quantity to study superconductivity [23]. However, the typical atomic-scale thickness and micron-scale lateral dimensions of these van der Waals superconductors make them challenging to measure with conventional methods, such as dielectric resonators [24], tunnel-diode-driven resonators [25], muon spin rotation [26], and the mutual inductance method [27].

Precise measurement of complex conductivity can act as a powerful tool to study the fundamental properties of superconductors [28]. The reactive component of the conductivity is the kinetic inductance, which arises from the kinetic energy of Cooper pairs. Kinetic inductance can directly measure superfluid stiffness and, therefore, has the capability to reveal quantum geometric contributions to stiffness which are invisible at the level of band dispersion [29–32], and for which there only exists indirect evidence at present [33] in twisted graphene. Sensitive measurements of the superfluid stiffness

*Present address: Northeastern University, Boston, MA; k.fong@northeastern.edu

Published by the American Physical Society under the terms of the Creative Commons Attribution 4.0 International license. Further distribution of this work must maintain attribution to the author(s) and the published article's title, journal citation, and DOI.

can also be used to detect the weak supercurrent dependence of the penetration depth (known as the nonlinear Meissner effect [34–37]), which offers highly constraining insights into the superconducting pairing symmetry. On the other hand, the resistive component of the complex conductivity reflects the energy dissipation due to normal-state carriers under the framework of the two-fluid model. Finally, kinetic inductance is an important ingredient in superconducting quantum circuitry: it can be used to engineer qubits [38], to realize high-sensitivity photon detectors [39], and to parametrically amplify signals with performance constrained solely by quantum noise [40,41].

In this paper, we describe an improved technique for accurately determining the kinetic inductance of these thin, small superconductor sample components. Inspired by the use of superconducting resonators in the readout of qubit states in circuit quantum electrodynamics (cQED), our method is a mesoscopic hybrid setup in which the kinetic inductance of our sample component acts as a small perturbation to the probe resonator. We then extract the relevant sample component parameters from the change of the resonator frequency and quality factor. This contrasts with previous kinetic inductance measurements in which a 50 Ω resistor shunts out the resonator in order to impedance match to the measurement circuitry, thus reducing the quality (Q) factor and sacrificing measurement sensitivity [42,43]. Our method shares the same fundamental mechanism as kinetic inductance detectors, which measure the suppression of resonance frequency due to the breaking of Cooper pairs in a superconducting resonator [39,44]. Already, this method has been applied to study the superfluid stiffness in superconductor-ferromagnet bilayers [45], $FeSe_{1-x}Te_x$ [46], and magic-angle twisted bilayer graphene [47], as well as metrological studies of the loss tangent of materials and the cleanliness of fabrication procedures to advance the development of superconducting quantum technology [48–52].

Here, we will first introduce the theory of kinetic inductance and superfluid stiffness, before focusing on the relevant hybrid resonator circuit model, deriving its corresponding formulas, and validating our method with a well-understood superconductor, i.e., Al. We then apply our hybrid resonator technique to measure the kinetic inductance of 2H–niobium diselenide ($NbSe_2$), thus demonstrating the effectiveness of our method on an exfoliated TMD superconductor. Along the way, we shall present the theory of kinetic inductance, clarifying the meaning and interpretation of these measurements. Some of the content has been discussed in previous works [49,52], but we will include the generic cases and interpret the formulas for practitioners in this growing field.

II. THEORY OF KINETIC INDUCTANCE AND SUPERFLUID STIFFNESS

In a superconductor, kinetic inductance arises from the inertial response of Cooper pairs to an applied current [53]. If all the Cooper pairs contribute to the supercurrent, we can equate the total kinetic energy to kinetic inductance and derive

$$L_K = \frac{m^*}{2n_s e^2}\left(\frac{l}{wt}\right), \tag{1}$$

where n_s is the superfluid density, t is the thickness of the sample component, and e and m^* are the charge and effective mass per quasiparticle, such that the mass of a Cooper pair is $2m^*$. The simple formula is insightful, but assumes Galilean invariance in order to relate superfluid density to kinetic inductance. This argument typically does not apply to real materials. More broadly, kinetic inductance measures the superfluid stiffness, $\mathcal{D}_s$. An applied current induces a vector potential $\mathbf{A}(\mathbf{r})$ inside the superconductor that leads to a gradient in the phase $\nabla\phi$ of the order parameter, $\Delta(\mathbf{r}) \to \Delta(\mathbf{r})\exp[i\,2e\mathbf{A}(\mathbf{r})\cdot\mathbf{r}/\hbar]$. The factor of 2 in the phase arises because the Cooper pairs involve two electrons, each of which picks up one unit of phase. The deformation costs energy ϵ, which is controlled by the stiffness

$$\epsilon = \int d^3r \mathcal{D}_s(\nabla\phi)^2, \tag{2}$$

and, hence, kinetic inductance can directly measure the cost of phase fluctuations. However, an exact relation between kinetic inductance and superfluid stiffness depends on details of the device. The subtleties arise from the difficulty of finding $\mathbf{A}(\mathbf{r})$ inside the superconductor, which can depend on sample geometry, London penetration depth, coherence length, and mean-free path (see the Appendix, Sec. A 1 for details). However, if we assume a uniform current profile that affects all Cooper pairs, we can derive the expression

$$L_K = \frac{1}{8}\left(\frac{\hbar^2}{e^2\mathcal{D}_s}\right)\left(\frac{l}{wt}\right), \tag{3}$$

which establishes a direct connection between superfluid stiffness and kinetic inductance.

Apart from the spatial profile of $\mathbf{A}(\mathbf{r})$, we have assumed both the locality and isotropy of the Mattis-Bardeen kernel [54] to relate the current density to the vector potential, as explained in the the Appendix, Sec. A 1,

$$J_\mu(\mathbf{r}) \propto \mathcal{D}_s\delta_{\mu\nu}\mathbf{A}_\nu(\mathbf{r}), \tag{4}$$

where μ, ν denote spatial directions. While the more general Mattis-Bardeen kernel offers a complete description, it complicates the analysis and obscures the relationship between kinetic inductance, penetration depth, and superfluid stiffness. Specifically, the superfluid stiffness is defined as the $\mathbf{q} = 0$ component of the Fourier transform of the Mattis-Bardeen kernel, $K(\mathbf{q})$ [28]. The penetration depth is derived from the solution of the nonlocal London equation [28], whereas the kinetic inductance characterizes an effective penetration depth that depends on both $K(\mathbf{q})$ and the boundary conditions [55]. Next, we address each assumption individually.

As we discuss in the Appendix, Sec. A 1, while the locality assumption might seem invalid for superconductors with large coherence lengths, practical factors such as sample thickness and electronic mean-free path strongly reinforce its validity. One may heuristically think of an effective coherence length that is dominated by the smallest of the electronic mean-free path and the sample thickness. As a result, despite the potential complications of a nonlocal kernel, the local approximation retains widespread applicability, particularly in thin samples.

In contrast, the breakdown of isotropic response in anisotropic superconductors is unavoidable. In these systems,

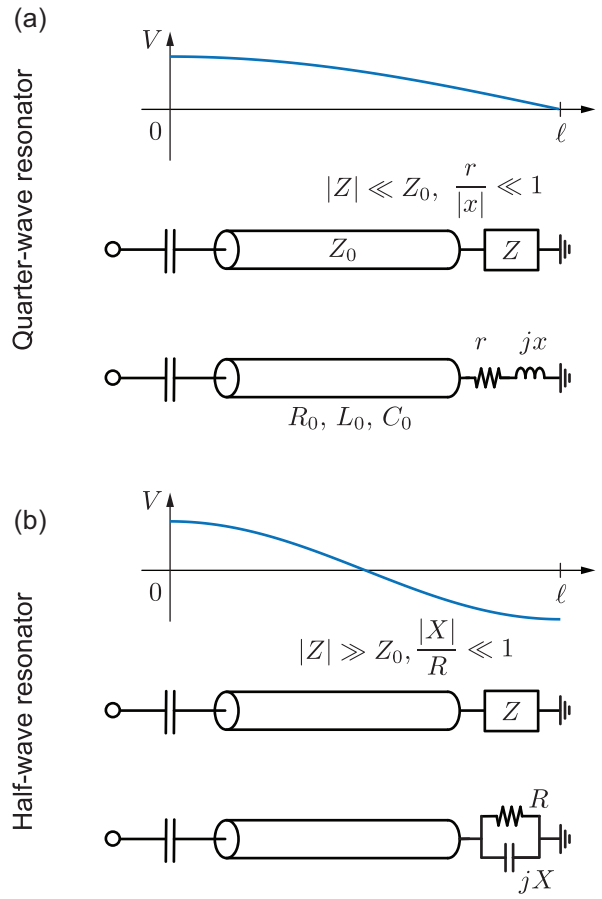

FIG. 1. Circuit model of (a) quarter-wave resonator and (b) half-wave resonator. The blue curve is a sketch of the magnitude of the voltage oscillations vs the distance from the coupling capacitor. ℓ is the physical length of the transmission line, schematically represented by the coaxial cable. The inductor or capacitor of interest with an impedance Z is embedded at the end of the transmission-line resonator to create a quarter-wave, for $|Z| \ll Z_0$, and half-wave, for $|Z| \gg Z_0$, resonator. Without loss of generality, $Z = r + jx = (1/R + 1/jX)^{-1}$.

the kinetic inductance depends on the alignment of current flow with the crystalline axes of the material. Beyond geometric factors related to the effective penetration volume (as detailed in the Appendix, Sec. A 1), the kinetic inductance picks up the penetration depth along the direction of the current.

III. DESCRIPTION OF THE MEASUREMENT METHOD AND CIRCUIT MODELING

Figure 1 shows a schematic representation of the transmission line resonator used to probe the sample component. The resonator is drawn as a coaxial cable of length ℓ and characteristic impedance Z_0. In practice, the resonator may consist of any transverse electromagnetic (TEM) or quasi-TEM transmission line, such as a microstrip or coplanar waveguide. Typically operating at radio and microwave frequencies, the resonator is coupled to the external circuitry via the capacitor on the left-hand side of the diagram. The sample with impedance Z terminates the resonator. We model the sample as an equivalent circuit with $Z = r + jx$, where $j = \sqrt{-1}$. The reactive component x modifies the resonance frequency, while the dissipative component r degrades the Q factor of the probe resonator by providing an additional channel for energy loss. The r accounts for loss in the sample and is agnostic to the origin of the dissipation, which can be due to the electrical contact, dielectric loss, or quasiparticles in the superconductors. The loss tangent, $\tan\delta$, of the sample component is defined to be $r/|x|$.

Below we analyze the circuit response using perturbation theory in two regimes. We first consider the case where $|Z| \ll Z_0$, which is the relevant case for measurements of kinetic inductance in superconducting samples. In such a case, the sample effectively shorts the resonator to ground, forming a quarter-wave resonator, and $Z = r + jx$, with $x = \omega L$ [Fig. 1(a)]. For completeness, we also consider the case where $|Z| \gg Z_0$, which will be of use for probing capacitive components. In this case, the sample effectively creates an open circuit, forming a half-wave resonator, and $1/Z = 1/R + 1/jX$, with $X = 1/\omega C$ [Fig. 1(b)]. In both cases, the quarter-wave and half-wave transmission-line resonators are equivalent to a lump parallel or series RLC resonator near their resonance frequencies, respectively [56], with R_0, L_0, and C_0 as the resistance, inductance, and capacitance of the probe resonators listed in the Appendix, Sec. A 2.

A. Quarter-wave resonator circuit model

Consider a quarter-wave transmission-line resonator of length ℓ connected to the ground plane without the sample component. The input impedance of the resonator can be computed [56] by means of the Telegrapher equations and is equivalent to that of a parallel RLC circuit with resonance frequency $\omega_0 = \pi v/2\ell$, where v is the velocity of light in the transmission line. The quality factor of the superconducting probe resonator, Q_0, is given by

$$Q_0 = \omega_0 R_0 C_0 = \frac{R_0}{\omega_0 L_0} = \frac{\pi}{4}\frac{1}{\alpha\ell}, \tag{5}$$

where α is the microwave attenuation per unit length of the transmission line. The microwave loss, which can be due to quasiparticles or two-level systems [48,50], is accounted for using the shunt resistor R_0 in the parallel RLC resonator model. A larger R_0 results in less electrical current going through the dissipative resistor and, thus, a higher Q_0.

Using the Telegrapher equation, the input impedance of the resonator now becomes

$$\begin{aligned} Z_{\text{in}} &= Z_0 \frac{(r + jx) + Z_0 \tanh(\alpha + jk)\ell}{Z_0 + (r + jx)\tanh(\alpha + jk)\ell} \\ &\simeq \frac{Z_0}{\alpha\ell + r/Z_0 - j\cot k\ell + jx/Z_0}, \end{aligned} \tag{6}$$

where k is the wave number. The approximation in Eq. (6) uses $|r + jx| \ll Z_0$, so that the sample component introduces only a small perturbation to the quarter-wave resonator impedance. By comparing the transmission-line resonator with the parallel RLC resonator and relating their physical parameters (see the Appendix, Sec. A 2), the loss becomes

$\alpha\ell + r/Z_0$ with a frequency shift $\delta\omega_0$ given by

$$\delta\omega_0 \simeq -\frac{2}{\pi}\frac{x}{Z_0}\omega_0. \tag{7}$$

The resonance-frequency shift is negative for an inductive sample, which effectively elongates the electrical length of the resonator.

The new internal quality factor Q_i, for the quarter-wave resonator with the sample component, becomes

$$\frac{1}{Q_i} = \frac{1}{Q_0} + \frac{1}{Q_{\text{eff}}}, \tag{8}$$

$$\text{where} \quad \frac{1}{Q_{\text{eff}}} = \frac{4}{\pi}\frac{r}{Z_0} = 2\left|\frac{\delta\omega_0}{\omega_0}\right|\tan\delta. \tag{9}$$

This Q_{eff} term has two contributions: the loss tangent of the sample component, $\tan\delta$, and the participation ratio $|\delta\omega_0/\omega_0|$, which weights it. The participation ratio is the ratio of energy stored in the sample component with respect to the total stored energy in the resonator [57]. A high Q_0 is necessary to reliably extract the loss of the sample component from the measurement of the Q_i. Using Eqs. (5) and (9), we can rewrite Eq. (8) as

$$\frac{1}{Q_i} = \frac{4}{\pi}Z_0\left(\frac{1}{R_0} + \frac{1}{Z_0^2/r}\right). \tag{10}$$

The loss from the reactive element effectively acts as a shunt resistor, of resistance Z_0^2/r, to the loss of the resonator, i.e., R_0.

B. Half-wave resonator circuit model

Similarly, we can compute the frequency shift and Q factor of the half-wave resonator terminated by the sample component. The Q factor of the bare, half-wave resonator is given by

$$Q_0 = \omega_0 R_0 C_0 = \frac{\omega_0 L_0}{R_0} = \frac{\pi}{2}\frac{1}{\alpha\ell}. \tag{11}$$

As before, we assume that the sample causes a small perturbation to the transmission-line resonator. For a capacitive sample with small loss tangent, we can further approximate that $R \simeq x/\tan\delta$ and $X \simeq x$. The input impedance of the half-wave resonator then becomes

$$Z_{\text{in}} = Z_0\frac{(1/R + 1/jX)^{-1} + Z_0\tanh(\alpha + jk)\ell}{Z_0 + (1/R + 1/jX)^{-1}\tanh(\alpha + jk)\ell} \simeq \frac{Z_0}{\alpha\ell + Z_0/R + j\tan k\ell - jZ_0/X}. \tag{12}$$

Comparing with the half-wave transmission-line equation [56], the loss becomes $\alpha\ell + Z_0/R$ with a frequency shift of

$$\delta\omega_0 \simeq \frac{1}{\pi}\frac{Z_0}{X}\omega_0, \tag{13}$$

i.e., $\delta\omega_0$ is positive (negative) if the element is inductive (capacitive), effectively shortening (elongating) the electrical length of the resonator—opposite the sign of the quarter-wave result [Eq. (7)].

The new Q_i of the half-wave resonator becomes

$$\frac{1}{Q_i} = \frac{1}{Q_0} + \frac{1}{Q_{\text{eff}}}, \tag{14}$$

$$\text{where} \quad \frac{1}{Q_{\text{eff}}} = \frac{2}{\pi}\frac{Z_0}{R} = 2\left|\frac{\delta\omega_0}{\omega_0}\right|\tan\delta. \tag{15}$$

This Q_{eff} term has two contributions: the loss tangent of the sample component, $\tan\delta$, and the participation ratio $|\delta\omega_0/\omega_0|$, which weights it. Moreover, the loss of the reactive element in a half-wave resonator r effectively acts as a shunt resistor R to that of the resonator, i.e., R_0. Using Eqs. (11) and (14), we can rewrite Eq. (15) as

$$\frac{1}{Q_i} = \frac{2}{\pi}Z_0\left(\frac{1}{R_0} + \frac{1}{R}\right). \tag{16}$$

Table I summarizes the formulas of the frequency shift and quality factor for both quarter-wave and half-wave resonators.

IV. VALIDATION OF CIRCUIT MODEL AND EXPERIMENTAL TECHNIQUE USING BCS THEORY

We validate the quarter-wave model developed above by measuring the kinetic inductance of a thin strip of Al, a well-known BCS superconductor, and then demonstrate the utility of this methodology by applying it to the exfoliated TMD superconductor $NbSe_2$. We report our measurements from five sample components: two Al strips and three exfoliated $NbSe_2$ strips. Their dimensions are listed in Table II.

A. Kinetic inductance of Al strip

The coplanar waveguide resonators in our experiments are fabricated using procedures that are conducive to measuring exfoliated flakes of superconductors while maintaining a high-Q factor [52]. The process begins with the fabrication of resonators by photolithography over a 240 nm sputtered-Nb film of about 2 kΩ sheet resistance on a float-zone silicon wafer. We use a CF_4 reactive ion to etch through the Nb film, followed by an oxygen etch to remove any NbF, and, lastly, an Ar etch to remove unwanted surface oxides. Holes are periodically etched into the Nb ground plane to trap stray flux vortices; oxygen plasma is used after photolithography to remove residual photoresist, which could otherwise cause Si pillars to form within the coplanar waveguide; buffered-oxide etch with hydrofluoric acid is used following the etching of the Si trenches to eliminate any remaining NbF resulting from CF_4 ion etching. Once the wafer is diced, electron-beam lithography and evaporation are used to deposit an 80-nm-thick Al strip, our sample component, onto an etched Si window at the end of the resonator.

Figure 2 displays the three coplanar waveguide resonators (from left to right): "reference," "control," and "sample" resonators. The three high-Q ($Q \sim 10^5$) resonators of prescribed lengths are capacitively coupled to a transmission feedline. The length of each resonator is designed to yield a resonance frequency in the range of 3–9 GHz, to match the cryogenic amplifier and circulator bandwidth. The choice of different

TABLE I. Formulas for quality factor and resonant-frequency shift.

	Quarter-wave resonator	Half-wave resonator
Resonant-frequency shift, $\delta\omega_0$	$\delta\omega_0 = -\frac{2}{\pi}\frac{x}{Z_0}\omega_0$	$\delta\omega_0 = \frac{1}{\pi}\frac{Z_0}{x}\omega_0$
Quality factor, Q_i	$\frac{1}{Q_i} = \frac{1}{Q_0} + \frac{1}{Q_{\text{eff}}}$ $= \frac{4}{\pi}Z_0\left(\frac{1}{R_0} + \frac{1}{Z_0^2/r}\right)$ $= \frac{1}{Q_0} + \frac{4}{\pi}\frac{\lvert x\rvert}{Z_0}\tan\delta$ $= \frac{1}{Q_0} + 2\left\lvert\frac{\delta\omega_0}{\omega_0}\right\rvert\tan\delta$	$\frac{1}{Q_i} = \frac{1}{Q_0} + \frac{1}{Q_{\text{eff}}}$ $= \frac{2}{\pi}Z_0\left(\frac{1}{R_0} + \frac{1}{R}\right)$ $= \frac{1}{Q_0} + \frac{2}{\pi}\frac{Z_0}{\lvert x\rvert}\tan\delta$ $= \frac{1}{Q_0} + 2\left\lvert\frac{\delta\omega_0}{\omega_0}\right\rvert\tan\delta$

resonance frequencies allows for measurement of multiple sample components per chip for each experimental cooldown. We also maximize the separation between reference and test resonator frequencies to help identify the correct resonator during measurement. When we are uncertain in identifying a resonance, we can temporarily eliminate the coplanar waveguide to the ground plane with a drop of silver epoxy, and recover it by dissolving the epoxy in an acetone bath.

The reference resonator on the far left in Fig. 2(a) is a half-wave resonator consisting only of Nb, with no additional material. Figure 2(b) displays the capacitive coupling between the resonators and the transmission line, which sets the resonators' coupling Q factor Q_c. By measuring the resonance frequency and Q factor of the reference resonators as a function of temperature, we quantify any background kinetic inductance and dissipation from the Nb resonators. Figures 2(c) and 2(d) show the Al patterns of the control

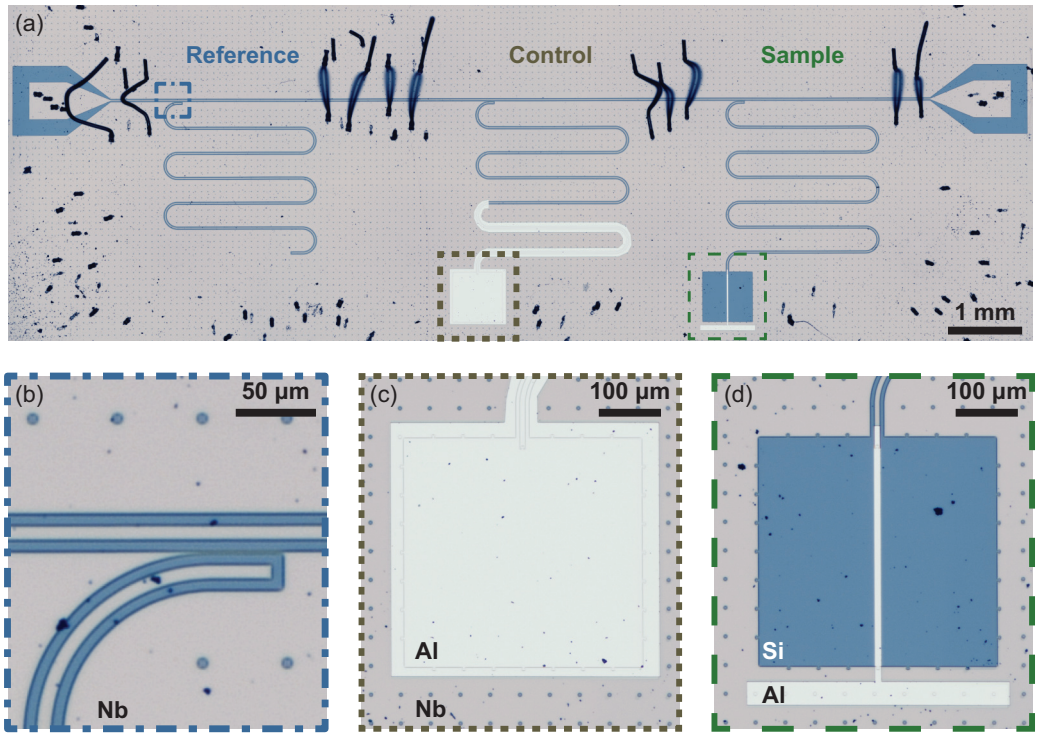

FIG. 2. (a) Optical image of three Nb coplanar waveguide resonators ("reference," "control," and "sample") capacitively coupled to a transmission feedline on a Si wafer surrounded by electromagnetic shielding within a dilution refrigerator. Wire bonds (black) connect the Nb ground plane above and below the feedline. (b) 100× magnification optical image of Nb reference resonator capacitively coupled to transmission feedline. (c) Quarter-wave control resonator with 80 nm of evaporated Al terminating the resonator to the ground plane. (a)–(d) Si hole arrays are used to pin vortices that may form in the superconducting Nb ground plane. (d) Quarter-wave sample resonator with 80-nm-thick sample strip of Al evaporated onto a Si window etched into the Nb, and terminated to the Nb ground plane.

TABLE II. Dimensions of sample components. Sample components presented in the main text are indicated by italics.

Sample	Width (μm)	Length (μm)	Thickness (nm)
	Al sample components		
KI06	10	420	80
KI07	10	420	80
	$NbSe_2$ sample components		
KI03	25 ± 3	37.7 ± 0.1	55.3 ± 0.4
KI19	8.2 ± 0.6	26.3 ± 0.2	36.0 ± 0.3
KI20	5.5	19.0	49 ± 0.5

and sample resonators, respectively. The control resonator is terminated directly to the ground plane without the long Al sample component that we intend to measure. The role of the control resonator is to monitor the temperature dependence of the frequency and quality factor of the niobium resonator used to measure our sample.

The resonators are cooled in a dilution refrigerator, inside a microwave package that is optimized to avoid undesired resonance modes near the designed resonance frequencies. The probe signal is sent through a highly attenuated coax cable to eliminate the thermal noise from room temperature. The signal then passes through the transmission bus line into the resonators where it interrogates the sample before proceeding to the cryogenic low-noise amplifier through a circulator (see the Appendix, Sec. A 3, for setup schematics). We measure the resonances from the scattering parameter S_{21}, which is defined as the ratio of the output to input voltage waves of the transmitted microwave signal through the feedline.

Figure 3 plots S_{21} of the sample component resonator over a range of temperatures from 20 to 840 mK. At the resonance frequency, the signal couples into the quarter-wave resonator, resulting in a sharp dip in S_{21}. We measured S_{21} for a range

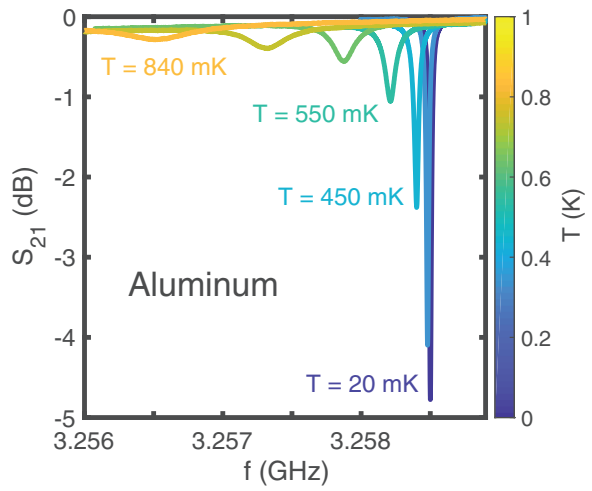

FIG. 3. Temperature-dependent S_{21} of the quarter-wave resonator containing an inductive strip of Al measured using a power of −50 dBm from the microwave source. The resonance frequency and loaded Q factor decrease with increasing temperature due to the increasing number of thermally excited quasiparticles.

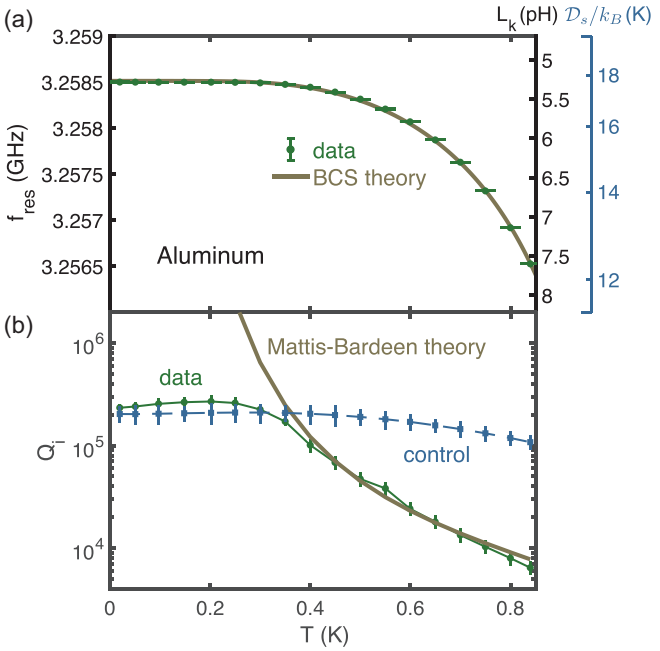

FIG. 4. (a) Resonance frequency (green data points) and (b) internal-Q factor Q_i of the quarter-wave resonator containing an Al sample component. (a) Solid brown curve is the best fit to BCS theory, i.e., Eqs. (17) and (18). Cooper pair density in Al decreases with increasing temperature, thus increasing kinetic inductance. The right y axis portrays the data as kinetic inductance in units of pH and $\mathcal{D}_s$ in units of K. (b) Using the fitted parameters in (a), we calculate Q_i according to the Mattis-Bardeen theory of surface impedance (solid brown line). The remarkable agreement to the data suggests that the degradation of Q_i for $T \geqslant 0.4\,\mathrm{K}$ is dominated by thermally excited quasiparticles in the sample component rather than the resonator because the corresponding drop in Q_i for the control resonator in the same temperature range is much smaller (blue dashed line). For $T < 0.4\,\mathrm{K}$, however, Q_i is potentially dominated by the resonator, not the Al strip.

of probe powers to ensure that the power is low enough and would cause no shift in the resonance frequency due to heating from the input power or nonlinearity from the Kerr effect. The resonance is sharpest at the lowest temperature and shows a gradual decrease in resonance frequency and Q factor as the temperature increases, due to the increase in kinetic inductance and dissipation, respectively.

To eliminate the effect of the microwave environment, including interference due to multiple reflections of the probe signal along the measurement chain, we analyze the S_{21} data using the circle fitting method [58] to extract the resonance frequency as well as the internal quality factor Q_i of the microwave resonator, which are plotted in Figs. 4(a) and 4(b), respectively. When applying the equation for the frequency shift of the quarter-wave resonator in Table I, we use the definition of $\Delta f = f(T) - f_0$ and $x = 2\pi f_0 L_K(T)$, where $f(T)$, f_0, and $L_K(T)$ are the resonance frequency at zero temperature, i.e., $T = 0\,\mathrm{K}$, and the kinetic inductance of the Al, respectively. Using Eq. (7), we have

$$f(T) = f_0\left(1 - 4\frac{f_0 L_K(T)}{Z_0}\right). \tag{17}$$

TABLE III. Fit parameters extracted from frequency data fitted to BCS theory for the Al sample component shown in Fig. 4(a).

Quantity	Fitted value	DC transport
f_0 (GHz)	3.263 ± 0.001	–
T_c (K)	1.195 ± 0.001	1.20 ± 0.01
$R_\square$ (mΩ)	109 ± 26	75 ± 20

To fit Eq. (17) to our data, we use BCS theory for the kinetic inductance [42],

$$L_K = \frac{l}{w}\frac{R_\square \hbar}{\pi \Delta}\coth\left(\frac{\Delta}{2k_B T}\right), \tag{18}$$

where $\hbar$ is the reduced Planck's constant, k_B the Boltzmann constant, T_c the critical temperature, $l = 420\ \mu$m the length, $w = 10\ \mu$m the width, $R_\square$ the sheet resistance, and Δ the BCS temperature-dependent gap energy of the Al strip. Using the approximation of $\Delta = \Delta_0[1-(T/T_c)^4]^{1/2}$ with $\Delta_0 = 1.764 \cdot k_B T_c$, we employ a least-squares fit of the data to Eq. (17) with three parameters, i.e., T_c, R_s, and f_0, and plot the result as the brown line in Fig. 4(a). We obtain f_0, the resonance frequency without the contribution of $L_K(T)$, from the fitting rather than the measured control resonator frequency because the resonance frequencies of lithographically identical resonators may vary by approximately 3 MHz, possibly due to slight fabrication differences or due to interaction between two resonances at the same frequency (see Fig. 10 in the Appendix, Sec. A 3). This statistical variance is slightly less than one part per thousand (ppt), but sizable when compared to the shift of resonance frequency induced by the kinetic inductance. This uncertainty in f_0 constitutes the limitation in accuracy of this measurement method. However, this measurement method has high precision, inherited from the high-Q factor of the resonators. As such, the error bar of the resonance frequency in Fig. 4(a) is less than one part per million (ppm).

Table III shows the fit parameters extracted from the BCS model. We can compare the fitted values of T_c and R_s with their respective measured values using DC transport on an Al film that was deposited alongside the resonator sample component. For the Al sample component, fit values are $T_c = 1.195 \pm 0.001$ K and $R_s = 109 \pm 26$ mΩ, which both overlap with the measured DC values of $T_c = 1.20 \pm 0.01$ K and $R_\square = 75.5 \pm 19.6$ mΩ. Using the fitted values, we calculate the kinetic inductance of the superconducting Al sample component and plot it on the right axis in Fig. 4(a). Equation (18) agrees well with the measured data. The zero-temperature kinetic inductance $L_{k0} \simeq 7$ pH, which is nearly 10^3 smaller than the equivalent inductance of the quarter-wave resonator, i.e., ≃2.9 nH, confirms that we are well within the perturbation regime and free to apply the equations in Table I.

As discussed above, measuring both $\mathcal{D}_s$ and Δ as a function of carrier density, temperature, magnetic field, and bias current is essential in revealing the true nature of superconductivity [22,43]. Using Eq. (3), we find that $\mathcal{D}_s/k_B$ [see right y axis of Fig. 4(a)] is of the order of a few Kelvins, i.e., $>\Delta_0/k_B$, suggesting that it takes more energy to create phase fluctuations than to break apart Cooper pairs in Al. We can further estimate the London penetration depth using

$$\lambda_L^2 = \frac{\hbar^2}{4\mu_0 e^2 \mathcal{D}_s} = 2\frac{wt}{l}\frac{L_K}{\mu_0}, \tag{19}$$

where μ_0 is the vacuum permeability, to be about 126 nm at $T \simeq 0$ K, in agreement with the λ_L obtained from similar resonator methods [55,59]. The applicability of the London equation to Al is somewhat surprising because its kinetic inductance could be in the anomalous limit (see the Appendix, Sec. A 1) due to its long coherence length and mean-free path. However, as we discussed above, the film thickness restricts the size of Cooper pairs and drives the thin film into a quasilocal limit [59].

By measuring the quality factors of the bare resonator and (Q_0) and the sample-terminated resonator (Q_i), we can infer the quality factor of the sample component (Q_{eff}). This value then yields the loss tangent δ [Eq. (9)] at the resonance frequency. The loss tangent $\tan\delta = \sigma_1/\sigma_2$ is equivalent to the ratio of the resistive and reactive components of the complex conductivity, $\sigma = \sigma_1 - j\sigma_2$. We note that here we follow the negative sign convention first introduced by Glover and Tinkham [60], wherein microwave photons were used to probe the complex conductivity. In fact, Glover and Tinkham also reported an observation of the superconducting energy gap in far-infrared measurements.

Figure 4(b) plots the measured Q_{i} of the sample resonator, along with that of a bare control resonator, vs temperature. The solid line shows the expected value of Q_{eff}, obtained by using the resonance shift from Fig. 4(a) and evaluating the Mattis-Bardeen integrals to obtain σ_1 and σ_2 at finite temperatures [54], where

$$\frac{1}{Q_{\text{eff}}} = 2\frac{\delta\omega_0}{\omega_0}\frac{\sigma_1}{\sigma_2}. \tag{20}$$

For $T \geqslant 0.4$ K, the measured Q_{i} closely follows the calculated Q_{eff}, indicating that increasing dissipation with increasing T is driven by a decrease in σ_2/σ_1 due to thermally excited quasiparticles from the breaking of Cooper pairs [61]. The close agreement between theory and experiment is remarkable because we use only the fitting parameters from the frequency shift to calculate σ_1 and σ_2. For $T < 0.4$ K, on the other hand, Q_{i} is limited by the quality factor of the transmission-line resonator, Q_0.

Examining the data below 0.4 K carefully, we observe that the measured Q_{i} slightly exceeds that of the control resonator and shows a minor peak near 0.2 K. This peak in Q_i is a key signature of the Q factor being limited by dissipation through two-level systems (TLSs). At temperatures well below $\hbar\omega_0/k_B$, the TLSs are in their ground states and ready to absorb photon energy from the measurement source. However, at temperatures well above $\hbar\omega_0/k_B$, the TLSs are already thermally excited out of their ground states, therefore reducing the probability of photon absorption and subsequent losses through the TLS channel. As a result, Q_i peaks at around $\hbar\omega_0/k_B$, i.e., 0.2 K for our sample component resonator, before its eventual degradation due to quasiparticles as temperature increases [62]. This minor peak in Q_i is suppressed when measuring the resonator with higher power because microwave photons from the measurement source can saturate the TLSs. The behavior of Q_i as a function of temperature at

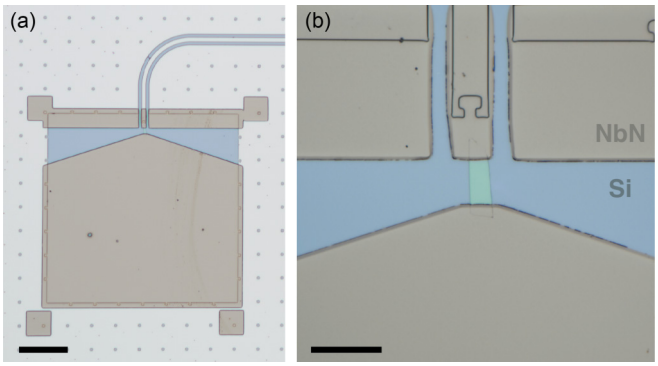

FIG. 5. Optical image of the niobium diselenide sample embedded in the quarter-wave resonator. (a) Grounding the coplanar waveguide resonator through an exfoliated strip of $NbSe_2$ sample using niobium nitride. The coplanar waveguide and the ground plane are made of Nb (light gray). (b) Close-up image of the $NbSe_2$ sample in a light-green color. The scale bars in (a) and (b) are 100 and 20 μm, respectively.

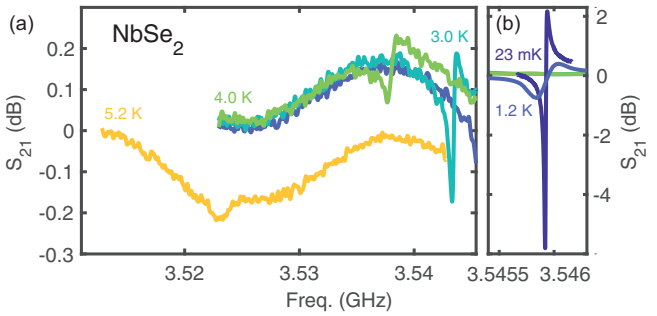

FIG. 6. Temperature-dependent Normalized S_{21} of a hybrid Nb-$NbSe_2$ quarter-wave resonator terminated by a 36-nm-thick inductive flake of $NbSe_2$ between the Nb resonator and Nb ground plane. Data are taken using a power of -50 dBm from the microwave source, before attenuation in the fridge lines. Resonance frequency and Q_i decrease with increasing temperature due to thermally excited quasiparticles.

various powers, plotted in Fig. 11 in the Appendix, Sec. A 3, follows this expectation.

B. Kinetic inductance of a niobium diselenide flake

We apply the above technique to measure the kinetic inductance of the layered superconductor 2*H*-niobium diselenide ($NbSe_2$). $NbSe_2$ belongs to the family of TMD superconductors and possesses many interesting properties. The Fermi surface consists of a set of pockets at Γ and K, which exhibit the nesting property [63,64], and features an anisotropic superconducting gap [25,65–67]. As the number of layers decreases, the transition temperature becomes gate tunable and drops from roughly 7.2 K to <5 K [68], potentially due to the increased role of fluctuations in the two-dimensional (2D) limit. Additionally, in the few-layer limit, evidence of nematicity setting in at T_c has been reported, suggestive of a subleading *p*- or *d*-wave state which coexists with the *s*-wave state observed in the bulk limit [69]. The locally noncentrosymmetric crystal structure results in strong spin-orbit coupling, believed to result in "Ising superconductivity" associated with high critical fields. In experiment, superconductivity is seen to persist up to the application of a ~35 T in-plane magnetic field [70]. Other interesting features of this system include the possible observation of a Fulde-Ferrell-Larkin-Ovchinnikov phase [71,72]. The kinetic inductance of few-layer-thick $NbSe_2$ gives further insight into the pairing symmetry and serves as proof of concept of our measurement technique as it applies to exfoliated vdW superconductors.

Figure 5 displays optical micrographs of an exfoliated $NbSe_2$ strip connected to a transmission-line resonator. The fabrication starts with mechanical exfoliation of $NbSe_2$ flakes onto SiO_2/Si substrates in an inert N_2 environment inside a glove box with oxygen levels lower than 0.5 ppm. We employ the dry pickup technique [73] using polycarbonate stamps to transfer $NbSe_2$ flakes from the SiO_2/Si to the destination area on a substrate with prepatterned Nb resonator structures. After removing polycarbonate residue with chloroform, we pattern the connection between the $NbSe_2$ flake and Nb transmission lines by electron-beam lithography. Next, we perform *in situ* Ar ion milling to remove surface oxide layers from the Nb resonator and $NbSe_2$ flake [Fig. 5(b)], followed by subsequent deposition of a 3-nm-thick Ti sticking layer and reactive sputtering of 200–240 nm of NbN to make galvanic connection between the two with negligible contact resistance [52]. We use a relatively thick NbN not only to ensure that it forms contact over the ~100–300 nm-thick $NbSe_2$, but also to reduce the contribution of kinetic inductance from NbN by suppressing its sheet resistance. In addition to the resonator shown in Fig. 5, each $NbSe_2$ device also consists of a Nb reference resonator and an Nb-NbN control resonator (see Fig. 17 in the Appendix). No aluminum is used for the $NbSe_2$ devices.

Figure 6 plots the scattering parameter of a hybrid Nb-$NbSe_2$ quarter-wave resonator containing the exfoliated $NbSe_2$ sample component. Similar to the Al-terminated resonator, both the resonance frequency and Q_i (see Fig. 8) decrease with increasing temperature. However, the change of the resonance frequency spans a higher temperature range than that shown in Fig. 4 for Al. This is commensurate with the higher transition temperature of $NbSe_2$, i.e., 7.06 K, measured by DC electrical transport (see Fig. 13 in the Appendix, Sec. A 3). At these temperatures, we also observe a frequency change for the control and reference resonators. This is expected because both Nb and NbN are superconducting materials with their own kinetic inductance. At temperatures well below their T_c values—measured to be 8.59 and 12.13 K, respectively—their kinetic inductances are negligible in our resonator design. However, at temperatures approaching the T_c of $NbSe_2$, the shift of the $NbSe_2$ resonance frequency includes a contribution from the change in kinetic inductance of the Nb transmission-line resonator.

Figure 7 plots the fractional frequency shift $\delta\omega/\omega_0$ vs temperature for the $NbSe_2$-terminated, control, and reference resonators. Since $\delta\omega/\omega_0$ follows the fractional change in inductance, we expect this quantity to track the temperature-dependent kinetic inductance in each resonator. Notably, $\delta\omega/\omega_0$ is the same for the control and reference resonators, even though their resonance frequencies are 3.680 and

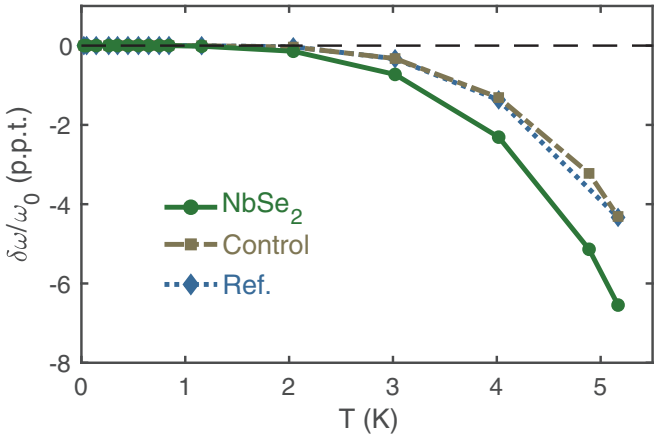

FIG. 7. Comparison of normalized frequency shift $\delta\omega/\omega_0$ of the three resonators in our $NbSe_2$ experiment. $\delta\omega_0/\omega_0$ of the control and reference resonator are about the same. This is noteworthy because their resonance frequencies are at 3.680 and 8.494 GHz, yet their normalized frequency shifts collapse to the same curve. We later extract the change in kinetic inductance of $NbSe_2$ absent any contribution from the change in kinetic inductance of the transmission-line resonator by taking the difference of their respective $\delta\omega_0/\omega_0$, as shown in Fig. 8.

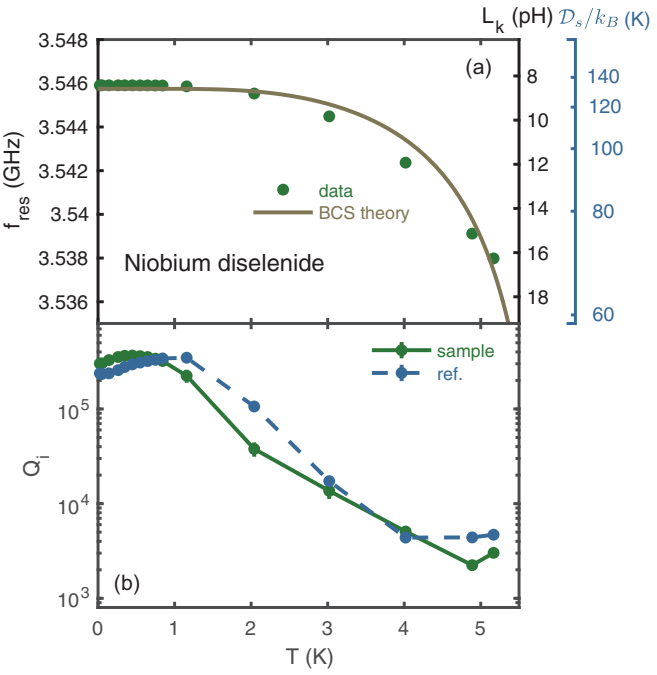

FIG. 8. (a) Comparison of measurement-extracted (dark-green marks) and BCS fit (brown line) kinetic inductance of $NbSe_2$, without contribution from control, as a function of temperature. The dark-green measured data are the difference of the normalized frequency shift of the control resonator and the hybrid Nb-$NbSe_2$ sample resonator. Cooper pair density in $NbSe_2$ decreases with increasing temperature, thus increasing kinetic inductance L_k and decreasing superfluid stiffness D_s. (b) Semilogarithmic plot of extracted internal quality factor (Q_i) as a function of temperature. The green curve corresponds to Q_i of the sample component resonator, whereas the blue dashed curve corresponds to Q_i of the reference resonator [see Fig. 2(b)].

8.494 GHz. This indicates that the change of their kinetic inductance at these temperatures is mostly due to the Nb. We can then extract $\delta\omega/\omega_0$ due to $NbSe_2$ kinetic inductance by subtracting the value for the control resonator from that of the $NbSe_2$-terminated resonator. Similar methods are used in resonator-based experiments [74].

Figure 8 plots the frequency of the $NbSe_2$ resonator vs temperature, with the contribution from the transmission-line subtracted. The coherence length of $NbSe_2$ is only roughly 10 nm and therefore sets the shortest length scale between coherence length (ζ) and penetration depth of the $NbSe_2$ sample flake. Consequently, the superconducting $NbSe_2$ is within the local limit ($\zeta \ll \lambda_L$) and we apply Eq. (19) in order to infer $\mathcal{D}_s$ and λ_L. As shown in the right y axis in Fig. 8(a), $\mathcal{D}_s/k_B$ remains larger than the T_c of $NbSe_2$. At the zero-temperature limit, $\lambda_L \approx 440$ nm, which is consistent with the reported values [25,26]. Any discrepancy between our reported value of penetration depth and previously reported values is probably due to the limitation of using Eq. (18) to describe the two-gap $NbSe_2$ superconductor, as well as error in the frequency subtraction.

Figure 8(b) plots Q_i of both the sample component and reference. Unlike in the temperature range plotted in Fig. 4(b), the Q_i of the reference resonators drops considerably because we are now closer to the T_c of Nb. In this temperature range, Q_i of the sample component and reference are approximately the same, suggesting that Q_i is dominated by the Q_0 term, rather than the Q_{eff} in Eq. (9). Since the participation ratio of the sample is merely a few ppt, the probe resonator quality factor Q_0 is too low for us to discern the true Q factor of the sample component. This substantiates the limitation of this measurement technique: Q_i is only representative of the loss through the sample component when $Q_0 \gg Q_{eff}$ in the perturbation regime in which the participation ratio of the sample component is small.

V. DISCUSSION AND CONCLUSION

Successful application of this technique requires some careful attention to detail. For example, to suppress the change of kinetic inductance from the superconducting materials used in fabricating the resonator, we sputter 200 nm of Nb to maintain a high geometric-to-kinetic inductance ratio. Nevertheless, as shown in Fig. 7, when the temperature approaches the T_c of Nb, the frequency shift of the coplanar waveguide resonator can become sizable and complicate the analysis for extracting the reactance and loss of the sample component. Therefore, we monitor both the control and reference resonators [Fig. 2(a)] to extract the kinetic inductance of the sample component and identify the applicable range of temperatures. We subtract the normalized frequency shift of the control resonator from that of the sample component resonator in order to extract the sample $NbSe_2$ kinetic inductance, but must note that this subtraction may be imperfect due to the inescapable fact that the control resonator is a separate physical object from the sample component resonator. As such, the normalized frequency shift due to the Nb resonator and

NbN stitching on the sample component resonator may not be exactly the same as a normalized frequency shift of the control resonator, which serves only as a proxy for the actual kinetic inductance contribution from the NbN and Nb of the sample component resonator. Furthermore, one must pay attention to the quality of the electrical contact between the resonator and sample component [52]. Extra contact resistance can degrade the Q factor and thus the measurement sensitivity. If the contact is composed of two different superconductors, the proximity effect may enhance or suppress the superconductivity of the sample component. Using superconductors with a short coherence length compared to the length of the sample component, such as NbN in stitching the $NbSe_2$ to the Nb resonator, can suppress the proximity effect in our measurements. If a Josephson junction were to form at the electrical contact, it would add an extra source of inductance and its critical current would set an additional limitation on the microwave power used in measuring the resonator. For kinetic inductance measurements, we should also consider any nonlocal effects and the relationship between relevant length scales, i.e., coherence length, mean-free path, and penetration depth. Fortunately, the typical thickness of exfoliated sample components generally keeps the measurement in the local limit. On the contrary, if the penetration depth is much smaller than the thickness of the sample, more calibration and theoretical calculations would be required to interpret the data from this technique.

In this paper, we present a model for using high-Q transmission-line resonators to measure the inductance or capacitance of a sample component to ppm precision, implement the model by measuring the kinetic inductance of a sample component strip of Al and a sample component flake of $NbSe_2$ using coplanar waveguide resonators, and validate both the model and its implementation by demonstrating agreement between our data and BCS theory for the kinetic inductance and Q factors of the Al and $NbSe_2$ sample components. The reported agreement between the data and BCS theory for the kinetic inductance and Q factor vouches for this method as a reliable technique, inviting interrogation of copious vdW materials, as demonstrated by the measurement of $NbSe_2$. Our method is enabled by advances in nanotechnology and quantum sensing and augments traditional techniques for measuring kinetic inductance by the technique of cQED. In addition, our method provides the enhanced capability of measuring both inductance and capacitance, and is now compatible with on-chip DC connections for electrical transport to control the chemical potential of the sample component with a gate, via the field effect [75]. Furthermore, we also include the measurement of dissipation, which can be understood from the imaginary and real components of the complex conductivity of a superconductor, and is extremely useful when studying losses in quantum devices [49]. Given its ability to measure mesoscopic flakes of vdW superconductors to ppm precision, this technique will be a highly functional tool in the rise of quantum materials and quantum sensing.

ACKNOWLEDGMENTS

We thank G. J. Ribeill for the helpful discussions, and M. Randeria and T. Lemberger for their insights and encouragement especially when we just started to have the idea. This work was supported by the STC Center for Integrated Quantum Materials, NSF Grant No. DMR-1231319. K.C.F., X.C., and J.H. acknowledge support from the Army Research Office under Contract No. W911NF-22-C-0021. J.B. and R.Q. acknowledges support from the NSF MRSEC program at Columbia University through the Center for Precision-Assembled Quantum Materials (Grant No. DMR-2011738). The authors acknowledge the use of facilities and instrumentation supported by NSF through the Columbia University, Columbia Nano Initiative, and the Materials Research Science and Engineering Center, Grant No. DMR-2011738.

APPENDIX

1. Theory of kinetic inductance and its relation to the penetration depth

In this section, we establish the theory behind the measurement of kinetic inductance. The kinetic inductance of a superconductor originates from the inertial response of Cooper pairs to the applied current, meaning that the energy of the system, $\epsilon = (1/2)L_K I^2$, must match the kinetic energy carried by the condensate. When a current is applied, a vector potential $\mathbf{A}(\mathbf{r})$ is induced within the superconductor, resulting in an electromagnetic energy,

$$\epsilon_{\rm EM} = \int d\mathbf{r}\, \mathbf{j}(\mathbf{r}) \cdot \mathbf{A}(\mathbf{r}) = \int d\mathbf{r}\, j_\mu(\mathbf{r}) A_\mu(\mathbf{r}), \tag{A1}$$

where $\mathbf{j}(\mathbf{r})$ is the current density and $\mu = x, y, z$ is a spatial index with an implied summation over repeated indices. The current that develops in response to the applied vector potential is related in linear response via

$$j_\mu(\mathbf{r}) = \int d\mathbf{r}'\, K_{\mu\nu}(\mathbf{r} - \mathbf{r}') A_\nu(\mathbf{r}'), \tag{A2}$$

where $K_{\mu\nu}(\mathbf{r} - \mathbf{r}')$ is the Mattis-Bardeen kernel [54]; this object is otherwise known as the current-current correlator and can be computed via standard means using the Kubo formula. The response is generically nonlocal, i.e., the current at position $\mathbf{r}$ depends on the vector potential at $\mathbf{r} \neq \mathbf{r}'$. The origin of nonlocality is that the response to an electromagnetic field of a superconductor is spread over a region of size determined by the coherence length ξ. In terms of Fourier components, this nonlocality brings in a variation in $K(\mathbf{q})$ at the scale of ξ.

By matching the electromagnetic energy stored to that of the inductor, we get a general formula of the kinetic inductance,

$$L_K = \frac{1}{2I^2} \int d\mathbf{r} d\mathbf{r}'\, K_{\mu\nu}(\mathbf{r} - \mathbf{r}') A_\mu(\mathbf{r}) A_\nu(\mathbf{r}'), \tag{A3}$$

in terms of the vector potential inside the superconductor $\mathbf{A}(\mathbf{r})$ and Mattis-Bardeen kernel $K_{\mu\nu}(\mathbf{r} - \mathbf{r}')$. As mentioned, there are standard methods for computing $K_{\mu\nu}$ in BCS theory, but computing the vector potential A inside the superconductor requires solving a boundary value problem.

The expression is much simpler if the Mattis-Bardeen kernel is assumed to be local and isotropic,

$$K_{\mu\nu}(\mathbf{r} - \mathbf{r}') = \frac{4e^2}{\hbar^2} \mathcal{D}_s \delta(\mathbf{r} - \mathbf{r}') \delta_{\mu\nu}, \tag{A4}$$

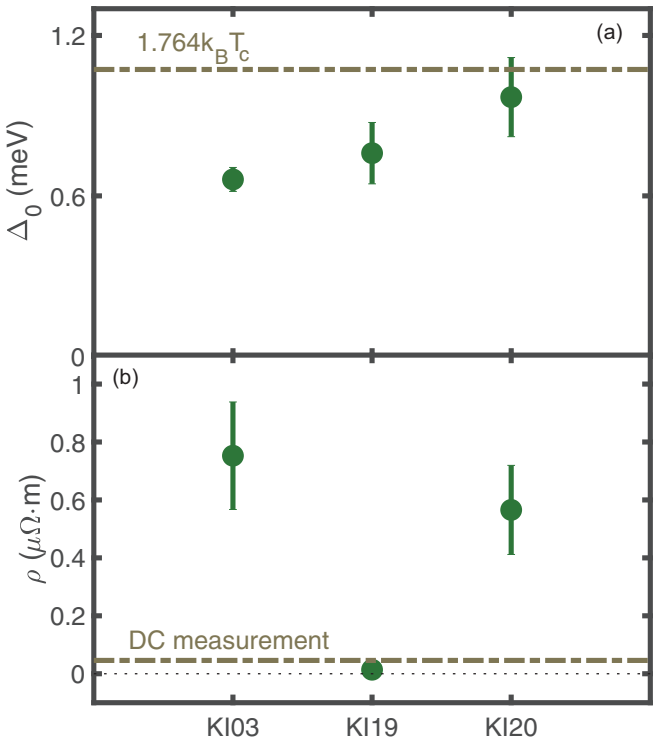

FIG. 9. Extracted BCS-fit parameter values of (a) zero-temperature gap energy Δ_0 (green points) and (b) resistivity ρ compared to measured values (dashed lines) from DC transport for three $NbSe_2$ exfoliated strips. Measured gap value in (a) is inferred from measured $T_c = 7.06$ K.

where $\mathcal{D}_s$ is the superfluid stiffness. This quantity is calculated by computing the momentum-dependent quantity $K_{\mu\nu}(\mathbf{q})$ and replacing it with its $q \to 0$ limit. This expression is valid in the limit where the coherence length ξ is much smaller than the London penetration depth; when ξ is large, the momentum dependence of $K_{\mu\nu}(\mathbf{q})$ can no longer be neglected. As for the vector potential, we can revert Eq. (A2) to write the kinetic

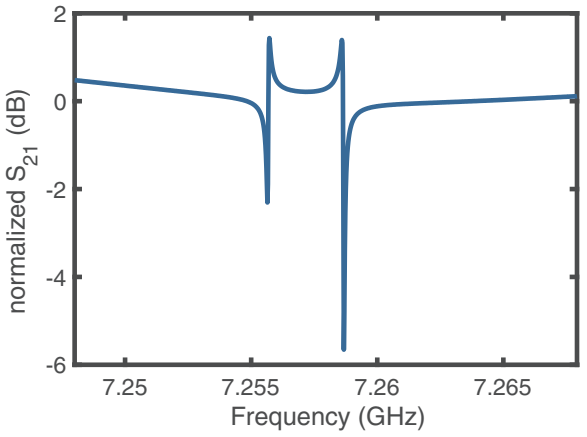

FIG. 10. Resonances of two coplanar waveguide resonators which are lithographically identical. The difference suggests sub-ppt level uncertainty between the resonance frequency design and actual implementation.

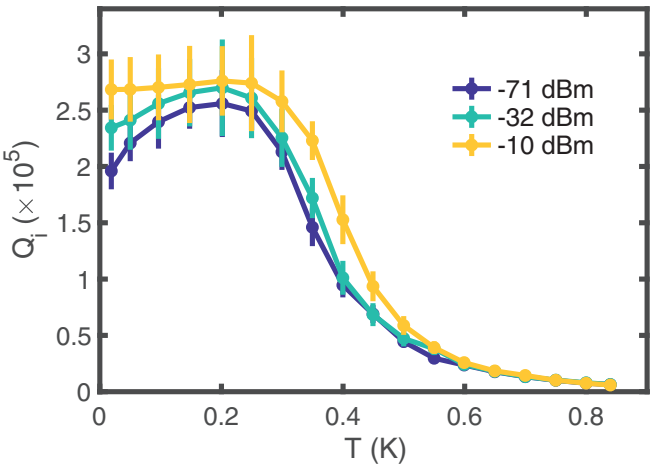

FIG. 11. Internal-Q factor Q_i of the Al-embedded sample component as a function of temperature at three different powers. The power in the legend denotes the power from the microwave source, before encountering attenuation in the fridge lines. At temperatures well below $\hbar\omega_0/k_B$, Q_i increases with power due to the saturation of two-level systems (TLSs) by the measurement power (see Fig. 12). When the TLSs saturate due to thermal excitations, Q_i has a maximum near $\hbar\omega_0/k_B$, i.e., around 0.2 K for our quarter-wave resonator. Q_i continues to decrease at higher temperatures because of dissipation from the Al sample component due to thermally excited quasiparticles, well described by Mattis-Bardeen theory (see Fig. 4).

inductance in terms of current density and then make the substitution

$$\int d\mathbf{r}\, j(\mathbf{r})^2 \to I^2\left(\frac{l^2}{V_{\text{eff}}}\right), \tag{A5}$$

where we have introduced V_{eff} as the penetration volume. It represents the volume of the sample where the current density is finite. Putting it all together, we get

$$L_K = \frac{1}{8}\frac{\hbar^2}{e^2\mathcal{D}_s}\left(\frac{l^2}{V_{\text{eff}}}\right) = \frac{\mu_0\lambda_L^2}{2}\left(\frac{l^2}{V_{\text{eff}}}\right). \tag{A6}$$

If the current density is present throughout the sample, which is the case for thin films ($t \ll \lambda_L$), the penetration volume is equal to the total volume ($= lwt$) and we recover Eq. (3). On the other hand, if the sample is too thick, current only flows close to the surface on a thin shell of size λ_L. This reduces the penetration volume to $2lw\lambda_L$ and the resulting kinetic inductance is given by $L_K = (l/w)\mu_0\lambda_L$. We can further solve the boundary value problem for arbitrary values of t/λ_L and interpolate between the two limits with

$$L_K = \frac{\mu_0\lambda_L}{4}\left(\frac{l}{w}\right)\coth\left(\frac{t}{2\lambda_L}\right). \tag{A7}$$

The idea of penetration volume is extremely useful in understanding anisotropic responses [76]. Anisotropic superconductors have a direction-dependent superfluid stiffness, that is, Eq. (A4) is modified to

$$K_{\mu\nu}(\mathbf{r}-\mathbf{r}') = \frac{4e^2}{\hbar^2}[\mathcal{D}_s]_\mu\delta(\mathbf{r}-\mathbf{r}')\delta_{\mu\nu}, \tag{A8}$$

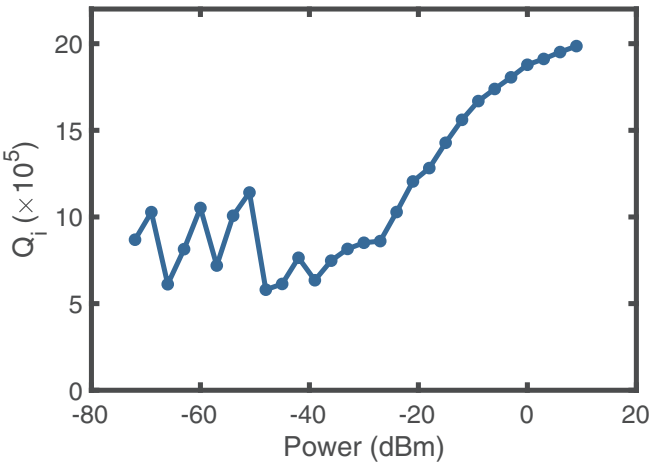

FIG. 12. Internal-Q factor Q_i of a reference resonator vs the microwave source power. At high powers, two-level systems (TLSs) are saturated by the power input to measure S_{21}, whereas at low powers, TLSs are in their ground state at low temperature, about 20 mK, available to transition to their excited state by absorbing photons from the resonator. Consequently, TLSs provide an additional loss channel through photon dissipation, which degrades Q_i. The scattering of Q_i at low power is due to the noise in measuring S_{21} when using a small power. The average number of photons in the resonator is of the order of one in the low-power regime of the plot, evinced by the leveling off of Q_i, typical in the single-photon limit.

which leads to a direction-dependent penetration depth $\lambda_{L,\mu}$ as well. Further, if μ denotes the direction of applied current, the element $[\mathcal{D}_s]_\mu$ is needed to relate the current density to the vector potential. In the limit of thin samples such that the penetration volume is the same as the volume of the device,

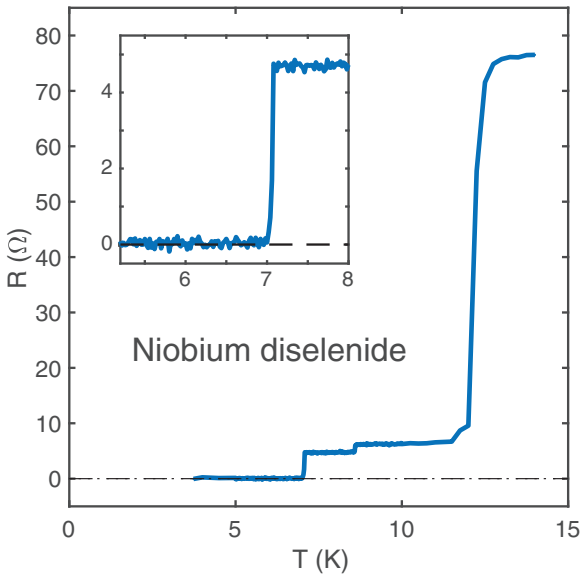

FIG. 13. DC resistance of $NbSe_2$, Nb, and NbN vs temperature measured in a $NbSe_2$-embedded resonator (sample component kinetic inductance 19) with T_c at 7.06, 8.59, and 12.13 K, respectively. Inset: Close-up of the $NbSe_2$ superconducting transition.

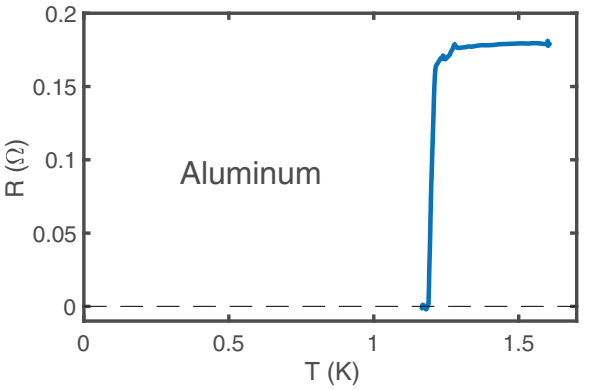

FIG. 14. Measured T_c of 80-nm-thick Al thin film deposited simultaneously with strip of Al sample component embedded in resonator, from main text.

the kinetic inductance then becomes

$$L_{K,\mu} = \left(\frac{l}{wt}\right)\frac{\mu_0\lambda_{L,\mu}^2}{2}, \tag{A9}$$

where the only difference from the previous expression is the additional index μ. More complications arise if the sample is thick such that fields do not entirely penetrate. The penetration volume for a thick slab is then given by

$$V_{\text{eff}} = 2(lw\lambda_c + lt\lambda_b + wt\lambda_a), \tag{A10}$$

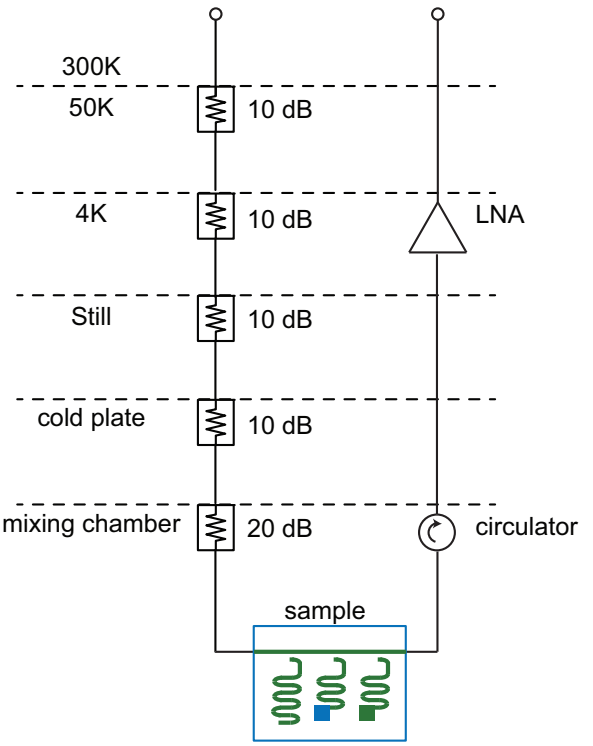

FIG. 15. Experimental setup of our kinetic inductance measurement. The attenuation of the microwave signal from room temperature to the mixing chamber is typically around 65 dB. A vector network analyzer is used to source and measure.

where, in general, $\lambda_a \neq \lambda_b \neq \lambda_c$. The kinetic inductance thus has a complicated dependence on the geometry of the device, including not only the dimensions but also aspect ratios [25,76].

Barring details of the device geometry, the local limit always connects the kinetic inductance to the penetration depth λ_L and, equivalently, the superfluid stiffness $\mathcal{D}_s$ as the two are related, $1/\lambda_L^2 = (4\mu_0 e^2/\hbar^2)\mathcal{D}_s$. This relation breaks down in the nonlocal regime where the coherence length is larger than the penetration depth—in this case, kinetic inductance measures an effective penetration depth which depends on $K(\mathbf{q})$ [55]. In this case, there are no simple analytic connections between the effective penetration depth and London penetration depth or superfluid stiffness.

It is worth mentioning that all our measurements fall in the local limit. In particular, the electronic mean-free path $l_{\rm mfp}$ restricts the size of Cooper pair in real space—heuristically, the mean-free path acts as an upper bound on the effective coherence length. Phenomenologically, it exponentially damps the Mattis-Bardeen kernel [54,77] $K(r) \to K(r)e^{-|r|/l_{\rm mfp}}$ and, hence, the short mean-free path can drive the system to a local limit, even if the BCS estimate of the coherence length is larger than the penetration depth. Similar arguments can be made for thin samples where the thickness controls the pair size [55].

2. Derivations of frequency shift and Q factor of resonance

a. Quarter-wave resonator

For the quarter-wave transmission-line resonator with the end connected directly to the ground plane without going through the sample component, the input impedance of the resonator is given by the Telegrapher equation [56],

$$Z_{\rm in} = Z_0 \tanh{(\alpha + j\beta)\ell}. \tag{A11}$$

For a wavelength λ of the microwave in the transmission line, $\beta = 2\pi/\lambda$. Using $\alpha\ell \ll 1$ for a high-Q superconducting resonator, Eq. (A11) becomes

$$Z_{\rm in} \simeq Z_0 \frac{1 - j\alpha\ell\cot\beta\ell}{\alpha\ell - j\cot\beta\ell}.$$

Near the resonance frequency ω_0, we can write the frequency ω as $\omega = \omega_0 + \Delta\omega$ so that when $\ell = \lambda/4$ in a quarter-wave resonator,

$$\cot\beta\ell \simeq -\frac{\pi}{2}\frac{\Delta\omega}{\omega_0}. \tag{A12}$$

Therefore,

$$Z_{\rm in} \simeq \frac{Z_0}{\alpha\ell + j\pi\Delta\omega/2\omega_0}. \tag{A13}$$

This equation has the same form as the impedance of a parallel RLC circuit, i.e., $[(1/R_0) + 2j\Delta\omega C_0]^{-1}$ with $\omega_0 = 1/\sqrt{L_0 C_0}$. By comparing the transmission-line resonator with the parallel RLC resonator, we can relate the physical parameters in these two models,

$$R_0 = \frac{Z_0}{\alpha\ell},$$
$$C_0 = \frac{\pi}{4}\frac{1}{\omega_0 Z_0}. \tag{A14}$$

The Q factor of the probe superconducting resonator, Q_0, is given by Eq. (5).

To quantify the kinetic inductance and loss of the sample component using a quarter-wave resonator, we compare Eqs. (6) and (A13) to find the frequency shift and change of Q factor by identifying

$$\alpha\ell \longrightarrow \alpha\ell + \frac{r}{Z_0}, \tag{A15}$$

$$\frac{\pi}{2}\frac{\Delta\omega}{\omega_0} \longrightarrow \frac{\pi}{2}\frac{\Delta\omega}{\omega_0} + \frac{x}{Z_0}, \tag{A16}$$

where the long arrow indicates a change in physical quantities from those of the pure quarter-wave resonator to those of the quarter-wave resonator connected to ground the plane via the sample component.

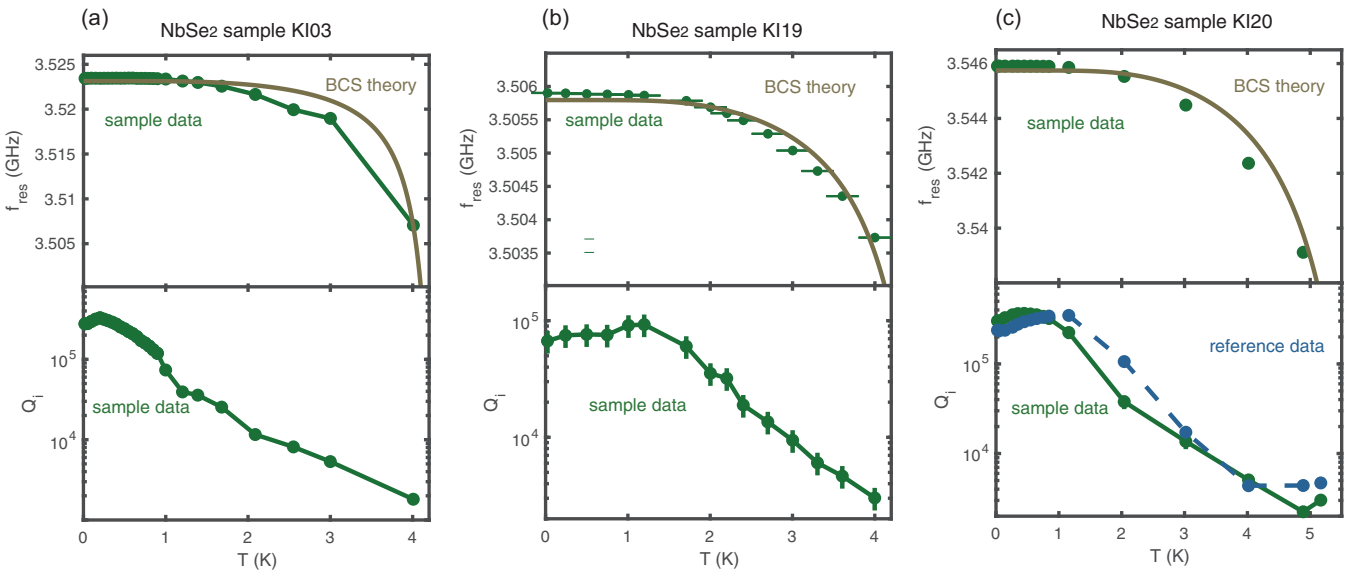

FIG. 16. Frequency and quality factor data for three different $NbSe_2$ samples.

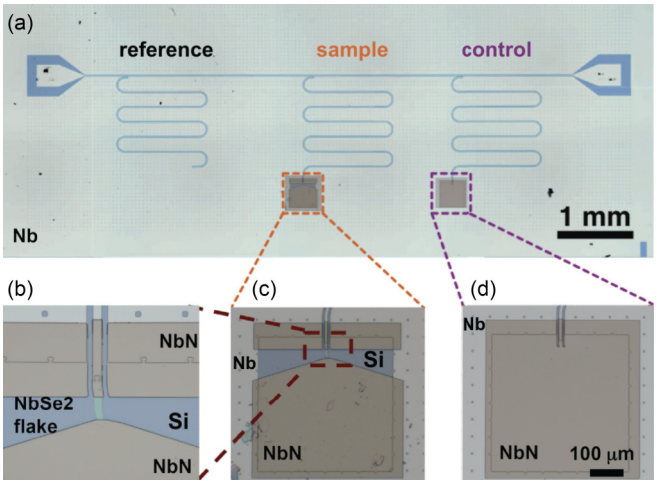

FIG. 17. Optical image of $NbSe_2$ device made from sputtered niobium and etched into three difference resonators: (a) reference, (b) sample, and (c) control. (a) is composed of niobium and silicon, (b) is a niobium resonator connected to an exfoliated flake of $NbSe_2$ via Ar ion milling followed by niobium nitride sputtering, and (c) is a niobium resonator with niobium nitride stitching used in (b), with no exfoliated flake.

b. Half-wave resonator

Similar to the analysis of the quarter-wave resonator, we will first consider the half-wave transmission-line resonator without the sample component. The input impedance is given by the Telegrapher equation [56],

$$Z_{\text{in}} = Z_0 \tanh(\alpha + j\beta)\ell \simeq \frac{Z_0}{\alpha\ell + j\tan\beta\ell}. \tag{A17}$$

Since $\ell = \lambda/2$ in a half-wave resonator,

$$\tan\beta\ell \simeq \pi\frac{\Delta\omega}{\omega_0}. \tag{A18}$$

Comparing the RLC circuit model, we have

$$R_0 = \frac{Z_0}{\alpha\ell}, \quad C_0 = \frac{\pi}{2}\frac{1}{\omega_0 Z_0}. \tag{A19}$$

The Q factor of the bare probe resonator is given by Eq. (11).

TABLE IV. Formulas of the equivalent R, L, and C of a transmission-line resonator [56].

	Quarter-wave resonator	Half-wave resonator
R_0	$\frac{Z_0}{\alpha\ell}$	$\frac{Z_0}{\alpha\ell}$
L_0	$\frac{4Z_0}{\pi\omega_0}$	$\frac{2Z_0}{\pi\omega_0}$
C_0	$\frac{\pi}{4\omega_0 Z_0}$	$\frac{\pi}{2\omega_0 Z_0}$

Comparing Eq. (12) with (A17),

$$\alpha\ell \longrightarrow \alpha\ell + \frac{Z_0}{R}, \tag{A20}$$

$$\pi\frac{\Delta\omega}{\omega_0} \longrightarrow \pi\frac{\Delta\omega}{\omega_0} - \frac{Z_0}{X}, \tag{A21}$$

we identify the frequency shift and new Q factor due to the sample component.

Table IV lists the equivalent R_0, L_0, and C_0 in the quarter-wave and half-wave resonators [56].

3. Supplementary information

Figures of additional information are listed as follows:

(1) Extracted BCS-fit parameter values of NbSe2 (Fig. 9). Resonances of two coplanar waveguide resonators which are lithographically identical to quantify fabrication error (Fig. 10).

(2) Internal-quality factor Q_i of the resonator with embedded Al sample component from Fig. 4 in the main text, measured under various microwave powers output from the microwave source, before any fridge line attenuation (Fig. 11).

(3) Internal-quality factor Q_i of a reference resonator versus microwave power from the microwave source at about 20 mK. This resonator is made of Nb without any sample component embedded (Fig. 12).

(4) DC electrical transport measurement of the transition temperature of $NbSe_2$, NbN (Fig. 13), and Al (Fig. 14) used in this experiment.

(5) Schematic of the experimental setup (Fig. 15).

(6) Frequency and quality factor temperature-dependence data for three separate $NbSe_2$ samples (Fig. 16).

(7) Optical image of $NbSe_2$ device including sample, reference, and control resonators (Fig. 17).

[1] Y. Cao, V. Fatemi, S. Fang, K. Watanabe, T. Taniguchi, E. Kaxiras, and P. Jarillo-Herrero, Unconventional superconductivity in magic-angle graphene superlattices, Nature (London) **556**, 43 (2018).

[2] X. Lu *et al.*, Superconductors, orbital magnets and correlated states in magic-angle bilayer graphene, Nature (London) **574**, 653 (2019).

[3] M. Yankowitz *et al.*, Tuning superconductivity in twisted bilayer graphene, Science **363**, 1059 (2019).

[4] J. M. Park, Y. Cao, K. Watanabe, T. Taniguchi, and P. Jarillo-Herrero, Tunable strongly coupled superconductivity in magic-angle twisted trilayer graphene, Nature (London) **590**, 249 (2021).

[5] Z. Hao *et al.*, Electric field–tunable superconductivity in alternating-twist magic-angle trilayer graphene, Science **371**, 1133 (2021).

[6] Y. Zhang *et al.*, Promotion of superconductivity in magic-angle graphene multilayers, Science **377**, 1538 (2022).

[7] L. Wang *et al.*, Correlated electronic phases in twisted bilayer transition metal dichalcogenides, Nat. Mater. **19**, 861 (2020).

[8] J. M. Park *et al.*, Robust superconductivity in magic-angle multilayer graphene family, Nat. Mater. **21**, 877 (2022).

[9] Y. Saito, T. Nojima, and Y. Iwasa, Highly crystalline 2D superconductors, Nat. Rev. Mater. **2**, 16094 (2016).

[10] S. Manzeli, D. Ovchinnikov, D. Pasquier, O. V. Yazyev, and A. Kis, 2D transition metal dichalcogenides, Nat. Rev. Mater. **2**, 17033 (2017).

[11] E. Y. Andrei *et al.*, The marvels of moiré materials, Nat. Rev. Mater. **6**, 201 (2021).

[12] H. Zhou *et al.*, Isospin magnetism and spin-polarized superconductivity in Bernal bilayer graphene, Science **375**, 774 (2022).

[13] Y. Zhang *et al.*, Enhanced superconductivity in spin-orbit proximitized bilayer graphene, Nature (London) **613**, 268 (2023).

[14] H. Zhou, T. Xie, T. Taniguchi, K. Watanabe, and A. F. Young, Superconductivity in rhombohedral trilayer graphene, Nature (London) **598**, 434 (2021).

[15] A. Ghiotto *et al.*, Quantum criticality in twisted transition metal dichalcogenides, Nature (London) **597**, 345 (2021).

[16] M. Oh *et al.*, Evidence for unconventional superconductivity in twisted bilayer graphene, Nature (London) **600**, 240 (2021).

[17] H. Kim *et al.*, Evidence for unconventional superconductivity in twisted trilayer graphene, Nature (London) **606**, 494 (2022).

[18] A. Banerjee *et al.*, Superfluid stiffness of twisted multilayer graphene superconductors, arXiv:2406.13742.

[19] D. Wong *et al.*, Cascade of electronic transitions in magic-angle twisted bilayer graphene, Nature (London) **582**, 198 (2020).

[20] U. Zondiner *et al.*, Cascade of phase transitions and Dirac revivals in magic-angle graphene, Nature (London) **582**, 203 (2020).

[21] E. Morissette *et al.*, Dirac revivals drive a resonance response in twisted bilayer graphene, Nat. Phys. **19**, 1156 (2023).

[22] V. J. Emery and S. A. Kivelson, Importance of phase fluctuations in superconductors with small superfluid density, Nature (London) **374**, 434 (1995).

[23] W. N. Hardy, D. A. Bonn, D. C. Morgan, R. Liang, and K. Zhang, Precision measurements of the temperature dependence of λ in $YBa_2Cu_3O_{6.95}$: Strong evidence for nodes in the gap function, Phys. Rev. Lett. **70**, 3999 (1993).

[24] S. Bae *et al.*, Dielectric resonator method for determining gap symmetry of superconductors through anisotropic nonlinear Meissner effect, Rev. Sci. Instrum. **90**, 043901 (2019).

[25] J. D. Fletcher, A. Carrington, P. Diener, P. Rodiere, J. P. Brison, R. Prozorov, T. Olheiser, and R. W. Giannetta, Penetration depth study of superconducting gap structure of 2H-$NbSe_2$, Phys. Rev. Lett. **98**, 057003 (2007).

[26] J. E. Sonier *et al.*, Muon-spin rotation measurements of the magnetic field dependence of the vortex-core radius and magnetic penetration depth in $NbSe_2$, Phys. Rev. Lett. **79**, 1742 (1997).

[27] I. Hetel, T. R. Lemberger, and M. Randeria, Quantum critical behaviour in the superfluid density of strongly underdoped ultrathin copper oxide films, Nat. Phys. **3**, 700 (2007).

[28] M. Tinkham, *Introduction to Superconductivity* (McGraw-Hill, New York, 1996).

[29] M. Tovmasyan, S. Peotta, P. Törmä, and S. D. Huber, Effective theory and emergent SU(2) symmetry in the flat bands of attractive Hubbard models, Phys. Rev. B **94**, 245149 (2016).

[30] A. Julku, S. Peotta, T. I. Vanhala, D.-H. Kim, and P. Törmä, Geometric origin of superfluidity in the lieb-lattice flat band, Phys. Rev. Lett. **117**, 045303 (2016).

[31] N. Verma, T. Hazra, and M. Randeria, Optical spectral weight, phase stiffness, and Tc bounds for trivial and topological flat band superconductors, Proc. Natl. Acad. Sci. USA **118**, e2106744118 (2021).

[32] P. Törmä, S. Peotta, and B. A. Bernevig, Superconductivity, superfluidity and quantum geometry in twisted multilayer systems, Nat. Rev. Phys. **4**, 528 (2022).

[33] H. Tian *et al.*, Evidence for Dirac flat band superconductivity enabled by quantum geometry, Nature (London) **614**, 440 (2023).

[34] S. K. Yip and J. A. Sauls, Nonlinear Meissner effect in CuO superconductors, Phys. Rev. Lett. **69**, 2264 (1992).

[35] D. Xu, S. K. Yip, and J. A. Sauls, Nonlinear Meissner effect in unconventional superconductors, Phys. Rev. B **51**, 16233 (1995).

[36] B. P. Stojković and O. T. Valls, Nonlinear supercurrent response in anisotropic superconductors, Phys. Rev. B **51**, 6049 (1995).

[37] J. A. Sauls, Theory of disordered superconductors with applications to nonlinear current response, Prog. Theor. Expt. Phys. **2022**, 033103 (2022).

[38] P. Winkel, K. Borisov, L. Grunhaupt, D. Rieger, M. Spiecker, F. Valenti, A.V. Ustinov, W. Wernsdorfer, and I. M. Pop, Implementation of a transmon qubit using superconducting granular aluminum, Phys. Rev. X **10**, 031032 (2020).

[39] P. Day, H. LeDuc, B. Mazin, A. Vayonakis, and J. Zmuidzinas, A broadband superconducting detector suitable for use in large arrays, Nature (London) **425**, 817 (2003).

[40] B. H. Eom, P. K. Day, H. G. Leduc, and J. Zmuidzinas, A wideband, low-noise superconducting amplifier with high dynamic range, Nat. Phys. **8**, 623 (2012).

[41] L. Ranzani *et al.*, Kinetic inductance traveling-wave amplifiers for multiplexed qubit readout, Appl. Phys. Lett. **113**, 242602 (2018).

[42] A. J. Annunziata *et al.*, Tunable superconducting nanoinductors, Nanotechnology **21**, 445202 (2010).

[43] G. Singh *et al.*, Competition between electron pairing and phase coherence in superconducting interfaces, Nat. Commun. **9**, 407 (2018).

[44] P. J. d. Visser, J. J. A. Baselmans, J. Bueno, N. Llombart, and T. M. Klapwijk, Fluctuations in the electron system of a superconductor exposed to a photon flux, Nat. Commun. **5**, 3130 (2014).

[45] C. G. L. Bøttcher *et al.*, Circuit quantum electrodynamics detection of induced two-fold anisotropic pairing in a hybrid superconductor–ferromagnet bilayer, Nat. Phys. **20**, 1609 (2024).

[46] N. T. Cherpak *et al.*, Possible manifestation of topological superconductivity and Majorana bound states in the microwave response of thin $FeSe_{1-x}Te_x$ film, arXiv:2312.11155.

[47] M. Tanaka *et al.*, Kinetic inductance, quantum geometry, and superconductivity in magic-angle twisted bilayer graphene, arXiv:2406.13740.

[48] J. M. Sage, V. Bolkhovsky, W. D. Oliver, B. Turek, and P. B. Welander, Study of loss in superconducting coplanar waveguide resonators, J. Appl. Phys. **109**, 063915 (2011).

[49] C. M. Quintana *et al.*, Characterization and reduction of microfabrication-induced decoherence in superconducting quantum circuits, Appl. Phys. Lett. **105**, 062601 (2014).

[50] L. Grünhaupt *et al.*, Loss mechanisms and quasiparticle dynamics in superconducting microwave resonators made of thin-film granular aluminum, Phys. Rev. Lett. **121**, 117001 (2018).

[51] C. R. H. McRae *et al.*, Cryogenic microwave loss in epitaxial Al/GaAs/Al trilayers for superconducting circuits, J. Appl. Phys. **129**, 025109 (2021).

[52] A. Antony *et al.*, Making high-quality quantum microwave devices with van der Waals superconductors, J. Phys.: Condens. Matter **34**, 103001 (2022).

[53] R. Meservey and P. M. Tedrow, Measurements of the kinetic inductance of superconducting linear structures, J. Appl. Phys. **40**, 2028 (1969).

[54] D. C. Mattis and J. Bardeen, Theory of the anomalous skin effect in normal and superconducting metals, Phys. Rev. **111**, 412 (1958).

[55] J. Gao, The physics of superconducting microwave resonators, Ph.D. thesis, California Institute of Technology, 2008.

[56] D. M. Pozar, *Microwave Engineering* (Wiley, 2005).

[57] Z. K. Minev *et al.*, Energy-participation quantization of Josephson circuits, npj Quantum Inf. **7**, 131 (2021).

[58] S. Probst, F. B. Song, P. A. Bushev, A. V. Ustinov, and M. Weides, Efficient and robust analysis of complex scattering data under noise in microwave resonators, Rev. Sci. Instrum. **86**, 024706 (2015).

[59] D. López-Núñez *et al.*, Magnetic penetration depth of aluminum thin films, arXiv:2311.14119.

[60] R. E. Glover and M. Tinkham, Conductivity of superconducting films for photon energies between 0.3 and $40kT_c$, Phys. Rev. **108**, 243 (1957).

[61] J. Gao *et al.*, Equivalence of the effects on the complex conductivity of superconductor due to temperature change and external pair breaking, J. Low Temp. Phys. **151**, 557 (2008).

[62] A. Alexander, C. G. Weddle, and C. J. K. Richardson, Power and temperature dependent model for high Q superconductors, arXiv:2205.06291.

[63] T. Yokoya *et al.*, Fermi surface sheet-dependent superconductivity in 2H-$NbSe_2$, Science **294**, 2518 (2001).

[64] M. D. Johannes, I. I. Mazin, and C. A. Howells, Fermi-surface nesting and the origin of the charge-density wave in $NbSe_2$, Phys. Rev. B **73**, 205102 (2006).

[65] Y. Noat *et al.*, Quasiparticle spectra of 2H-$NbSe_2$: Two-band superconductivity and the role of tunneling selectivity, Phys. Rev. B **92**, 134510 (2015).

[66] E. Khestanova, J. Birkbeck, M. Zhu, Y. Cao, and G. Y. Nano, Unusual suppression of the superconducting energy gap and critical temperature in atomically thin $NbSe_2$, Nano Lett. **18**, 2623 (2018).

[67] T. Dvir *et al.*, Spectroscopy of bulk and few-layer superconducting $NbSe_2$ with van der Waals tunnel junctions, Nat. Commun. **9**, 598 (2018).

[68] R. F. Frindt, Superconductivity in ultrathin $NbSe_2$ layers, Phys. Rev. Lett. **28**, 299 (1972).

[69] A. Hamill *et al.*, Twofold symmetric superconductivity in few-layer $NbSe_2$, Nat. Phys. **17**, 949 (2021).

[70] X. Xi *et al.*, Ising pairing in superconducting $NbSe_2$ atomic layers, Nat. Phys. **12**, 139 (2016).

[71] P. Wan *et al.*, Orbital Fulde-Ferrell-Larkin-Ovchinnikov state in an Ising superconductor, Nature (London) **619**, 46 (2023).

[72] X. Liu, Y. X. Chong, R. Sharma, and J. C. S. Davis, Discovery of a Cooper-pair density wave state in a transition-metal dichalcogenide, Science **372**, 1447 (2021).

[73] L. Wang *et al.*, One-dimensional electrical contact to a two-dimensional material, Science **342**, 614 (2013).

[74] K. Cho, H. Kim, M. A. Tanatar, J. Hu, B. Qian, Z. Q. Mao, and R. Prozorov, Precision global measurements of London penetration depth in $FeTe_{0.58}Se_{0.42}$, Phys. Rev. B **84**, 174502 (2011).

[75] G.-H. Lee *et al.*, Graphene-based Josephson junction microwave bolometer, Nature (London) **586**, 42 (2020).

[76] R. Prozorov *et al.*, Measurements of the absolute value of the penetration depth in high-Tc superconductors using a low-Tc superconductive coating, Appl. Phys. Lett. **77**, 4202 (2000).

[77] G. Seibold, L. Benfatto, and C. Castellani, Application of the Mattis-Bardeen theory in strongly disordered superconductors, Phys. Rev. B **96**, 144507 (2017).